Optics & Laser Technology 167 (2023) 109844

Contents lists available at ScienceDirect

Optics and Laser Technology

journal homepage: www.elsevier.com/locate/optlastec

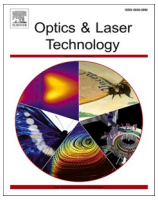

Full length article

A terahertz Janus metastructure with a multi-function of different logic gates and multiple physical quantities detection

Jiahao Zou, Junyang Sui, Qi Chen, Yuxin Wei, Hai-Feng Zhang *

College of Electronic and Optical Engineering & College of Flexible Electronics (Future Technology), Nanjing University of Posts and Telecommunications, Nanjing 210023, China

ARTICLE INFO

Keywords:
Metastructure
Janus metastructure
Multi-function
Logic gate
Physical quantities detection

ABSTRACT

In this paper, a Janus metastructure (JM) is given, which can realize the multi-function of different logic gates and detection of multiple physical quantities such as magnetic field, angle, and refractive index on the positive and negative scales. Furthermore, the multiscale sensing is also controlled by the logic gate. By varying the two different magnetic fields applied to the specific medium layers, the sharp absorption peak (AP), which is modulated by the external magnetic fields, is obtained in the terahertz (THz) range. The emergence of AP follows NOR logic and AND logic gates, on the positive and negative scale respectively. The results demonstrate that the frequency point (FP) of AP will fluctuate in response to the changes in the detection of physical quantities. Consequently, it is possible to accomplish physical quantities sensing functionalities by determining the FP of AP. The JM, proposed in this paper, provides a new research idea and has a more promising future. Its detection ranges of refractive index, tiny angular changes and magnetic field are 0.61 ~ 0.65 T or 1.185 ~ 1.2 T, 1.4 ~ 1.9 degrees or 2.9 ~ 3 degrees, and 1.05 ~ 1.45 or 2.1 ~ 2.5, which can be widely used in biomedical and physical fields.

1. Introduction

The study of Janus metastructure (JM) in the fields of electromagnetism, optics, and photonics is quite significant [1–6]. These materials have a periodic structure of refractive index that allows them to manipulate electromagnetic waves (EWs) in unique ways [7]. Similar to how electronic band gaps exist in crystalline solids, the one-dimensional (1-D) metastructures can exhibit photonic band gaps (PBGs), in which EWs cannot propagate through the material [8,8]. However, many studies have proved that the symmetry of JM will be destroyed when the defect layer is introduced [9]. It changes the band structure of JM and generates new electromagnetic patterns within the PBG so that EWs can propagate in JM at specific frequency bands [10]. JM is useful for applications such as optical filtering [11], waveguiding [12], and logic gates [13,14]. Especially, in the research field of sensing, many innovative and prospective works have been proposed [15–18]. JMs also have the potential for use in developing new types of optical devices and technologies, including photonic circuits and quantum optics [19–21].

Indium Antimonide (InSb) is a semiconductor material with unique properties that make it useful for a wide range of applications in electronics, optoelectronics, and thermoelectric devices [22,23]. It is a high electron mobility semiconductor material. InSb can be used as the defect layer in JM because of its dispersion and gyratory properties, as well as the magneto-optical effect it displays when magnetic fields are applied [24].

As the research continues to advance, metastructure devices that can be used for logic gates and physical quantities detection are widely studied. Parandin *et al.* [25] designed an all-optical JM with the functions of NOR and AND logic gates. Ghorbani *et al.* [26] presented a new metastructure biosensor based on numerical methods for glucose concentration monitoring in different samples. A magnetic field sensor capacity of 1-D JM was investigated by Atalay *et al.* [27]. In the field of the development of computer logic calculation and physical detection, these works are of great significance. But, these studies only have a single function and did not integrate logic gates and physical quantities detection. This will limit the research ideas in related fields. The JM integrating logic gates and physical quantities detection has broad space for development and can be adapted to various application scenarios, including smart homes, industrial automation, medical devices, transportation, and more [1,2].

* Corresponding author.
E-mail addresses: hanlor@163.com, hanlor@njupt.edu.cn (H.-F. Zhang).

https://doi.org/10.1016/j.optlastec.2023.109844
Received 15 May 2023; Received in revised form 3 June 2023; Accepted 14 July 2023
Available online 23 July 2023

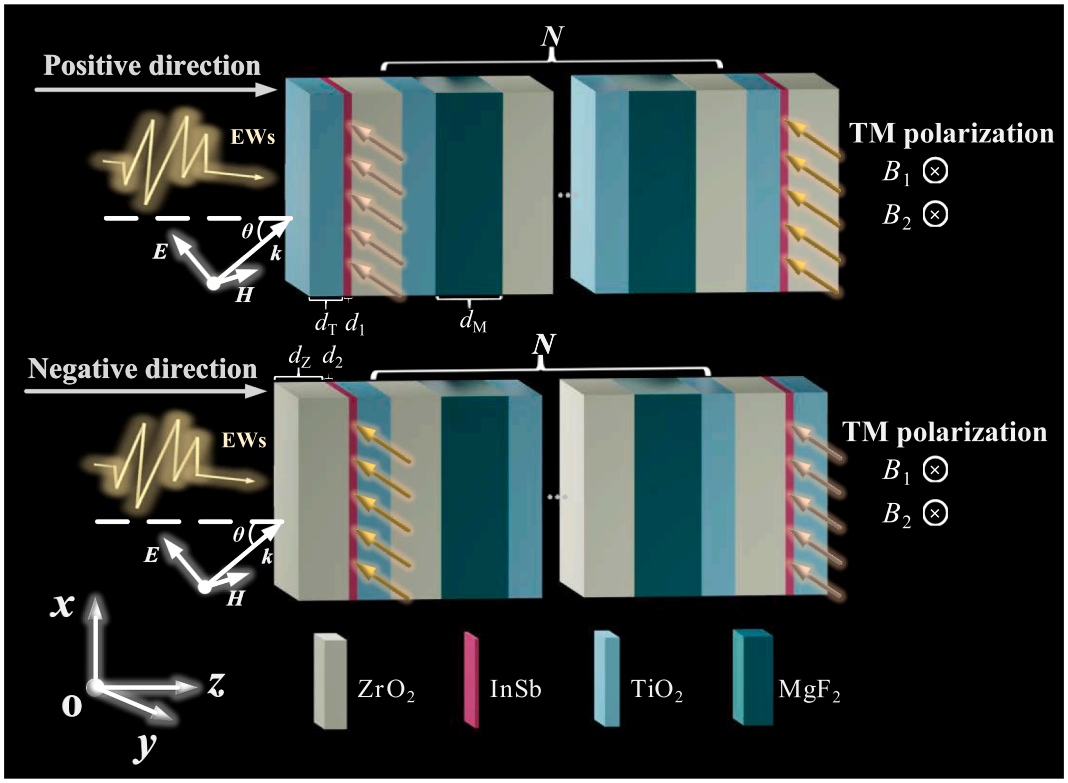

Fig. 1. Schematic diagram of the proposed JM which is made up of different dielectric layers. Two beams of EWs are incident from the positive and negative directions. The directions of the applied magnetic fields are marked with the coordinate axis as the reference.

In this paper, a 1-D JM has been given. It incorporates the logic gate and physical amount-detecting capabilities. To break the symmetry of JM and create a sharp absorption peak (AP) with a high-quality factor (*Q*), magnetized InSb is used as a defect layer. By controlling applied magnetic fields, it is possible to identify whether an AP is present or absent when its value is>0.9, accomplishing the logic gate function. The frequency point (FP) corresponding to the AP will move when the applied magnetic field and the refractive index (RI) of the medium layers vary. And it possesses a strong linear fitting relationship (LFR), a high figure of merit (*FOM*), and a high *Q*. The detection of slight changes in the magnetic field or the RI is possible thanks to the position of the AP. Moreover, because of the magneto-optical effect of InSb, with the changes of EWs incidence angle θ, the FP corresponding to AP will also change. So that the sensing of θ also can be achieved.

2. Structure design and simulation

Fig. 1 depicts the 1-D JM that can be created using the etching approach [28], which is made up of ordinary Titanium Dioxide (TiO_2), Zirconium Dioxide (ZrO_2), and Magnesium Fluoride (MgF_2) medium for non-symmetrical arrangement. The JM has a periodic structure, and the numbers of the period N are $N = 6$. Additionally, the magneto-optical medium InSb layers are added as flaws to the initial structure, and its entire construction is exposed to 300 K of air to adapt to the general environment. Different mediums are filled here with various colors to represent them. In this paper, the normalized thickness d_0 is used and its value is 8 μm. The thicknesses of the ordinary medium TiO_2, ZrO_2, and MgF_2 are severally replaced by d_T, d_Z, and d_M, and the parameter values of each other are $4d_0$, $6d_0$, and $8d_0$. The values of RI of these ordinary media are respectively $n_T = 2.76$, $n_Z = 2.4$, and $n_M = 1.38$. Due to the influence of the external magnetic field, the dielectric of InSb behaves as an anisotropic tensor, and as a result, its RI fluctuates with the strength of the magnetic field. The defect layers are made up of two semiconductors, $InSb_1$ and $InSb_2$, whose thicknesses respectively are $d_1 = d_0$ and $d_2 = d_0$. B_1 and B_2 ($B_1 = 0.65$ T, $B_2 = 1.2$ T) are the external magnetic field applied vertically on $InSb_1$ and $InSb_2$ along the *y*-axis. In addition, the theoretical model is the main focus study. Conventional mediums are unaffected by the external magnetic field, and in contrast to regular dielectric layers, InSb layers are exceedingly thin. Since other InSb layers are unaffected, the magnetic field area exerted on the particular InSb layer is tiny.

Taking into account the experimental use, Xuan *et al.* [29] designed a gradient magnetic field coil. A spatial linear magnetic field can be produced by applying current to it, which satisfies the demands of this work that the magnetic field strengths on various InSb layers are different and that the effects of nearby magnetic fields be isolated.

The dielectric constant of InSb can be calculate by the matrix of its dielectric function [30,31]:

$$\boldsymbol{\varepsilon}_{\mathrm{Insb}} = \begin{pmatrix} \varepsilon_x & 0 & \varepsilon_{xz} \\ 0 & \varepsilon_y & 0 \\ -\varepsilon_{xz} & 0 & \varepsilon_x \end{pmatrix}, \tag{1}$$

where [30,31]

$$\varepsilon_x = \varepsilon_\infty - \varepsilon_\infty \frac{\omega_p^2(\omega + i\nu_c)}{\omega[(\omega + i\nu_c)^2 - \omega_c^2]}, \tag{2}$$

$$\varepsilon_y = \varepsilon_\infty - \varepsilon_\infty \frac{\omega_p^2}{\omega(\omega + i\nu_c)}, \tag{3}$$

$$\varepsilon_{xz} = \varepsilon_\infty \frac{i\omega_p^2\omega_c}{\omega[(\omega + i\nu_c)^2 - \omega_c^2]}. \tag{4}$$

Among them, i=(-1)$^{-1/2}$, ε_∞=15.68 is the high-frequency limit dielectric constant [32], $\omega_p = ne^2/\varepsilon_0 m^*$is the plasma frequency, ε_0 and e respectively represent the dielectric constant, and electron charge in the vacuum. $m^*$is the effective mass of the carrier, which is related to the mass of the electron m_e. For InSb, m^*=0.015m_e. As Eq.(6) shows, n, the

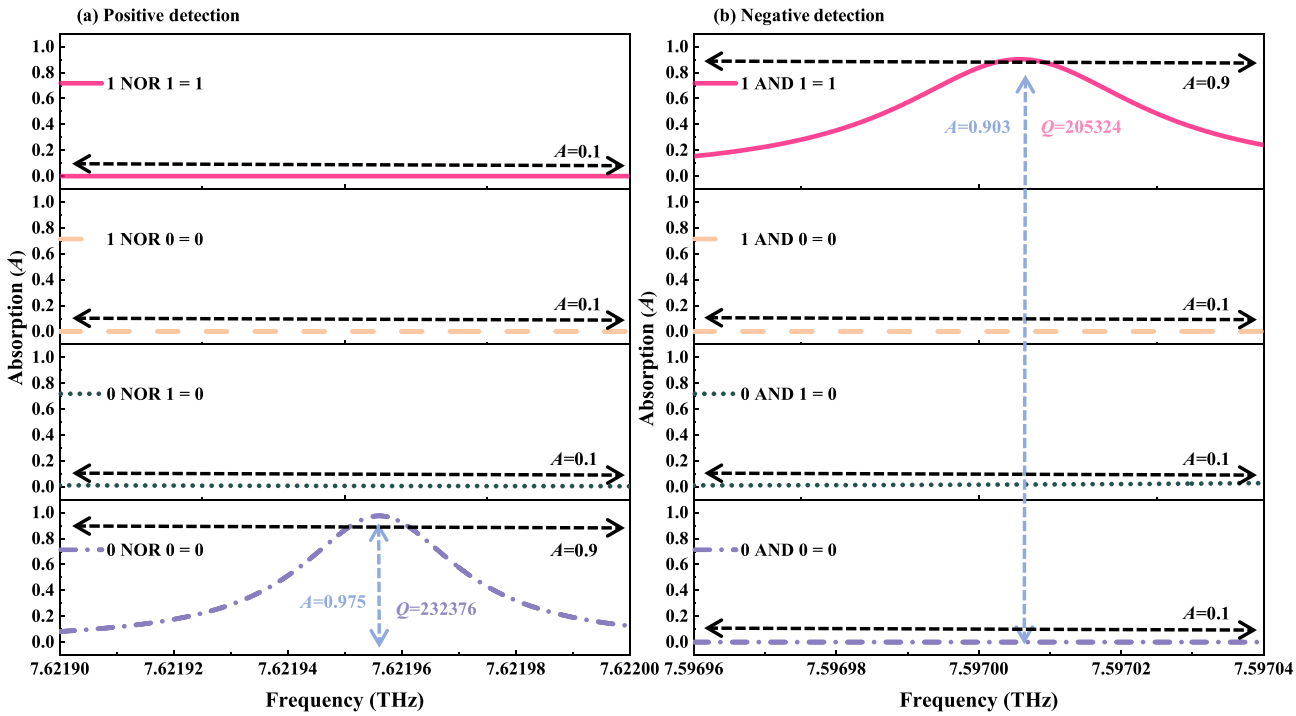

Fig. 2. Schematic diagrams of magnetically controlled logic gate operations and AP when EWs propagate. (a) The positive scale NOR logic operation and corresponding AP under magnetic field. (b) The negative scale AND logic operation and corresponding AP under magnetic control.

intrinsic carrier density, plays a critical role in the dielectric properties of InSb. ν_c is the collision frequency of the carrier and the value of the ν_c of $InSb_1$ and $InSb_2$ is $1 \times 10^{-4}\omega_p$ [30,31]. The electron gyration frequency, which is proportional to the intensity of the applied electric field, is given by the formula $\omega_c = eB/m^*$ [30,31].

$$n(m^{-3}) = 5.76 \times 10^{20} T_0^{1.5} \exp[-0.26/(2 \times 8.625 \times 10^{-5} \times T_0)], \tag{5}$$

the equation shows that the temperature T_0 has a significant impact on it.

When an external magnetic field is applied, the external magnetic field primarily controls the TM polarization of the EWs while not affecting the TE polarization. The findings demonstrate that the parameters of the 1-D JM based on InSb under magnetization are identical to those under unmagnetization [33]. As a result, this work will exclusively explore JM performance under TM polarization and use the transfer matrix approach to analyze the overall structure [34,35]. For TM polarization, the anisotropic material effective dielectric constant of InSb is stated as [36]:

$$\varepsilon_{\mathrm{TM}} = \frac{\varepsilon_x^2 - \varepsilon_{xz}^2}{\varepsilon_x^2}, \tag{6}$$

Moreover, the RI of InSb is $n_{\mathrm{TM}}=(\varepsilon_{\mathrm{TM}})^{1/2}$. Under TM polarization, the transfer matrix of InSb is expressed as [35]:

$$\mathbf{M}_{\mathrm{TM}k} = \begin{pmatrix} \cos(k_{kz}d_k) + \frac{k_{kx}\varepsilon_{xz}}{k_{kz}\varepsilon_x}\sin(k_{kz}d_k) & -\frac{i}{\eta_k}\left[1 + \left(\frac{k_{kx}\varepsilon_{xz}}{k_{kz}\varepsilon_x}\right)^2\right]\sin(k_{kz}d_k) \\ -i\eta_k \sin(k_{kz}d_k) & \cos(k_{kz}d_k) - \frac{k_{kx}\varepsilon_{xz}}{k_{kz}\varepsilon_x}\sin(k_{kz}d_k) \end{pmatrix}, \tag{7}$$

where $k_{kx} = \omega/cn_{\mathrm{TM}}\sin\theta_k$ is the component of the wave vector on the x-axis, $k_{kz} = \omega/cn_{\mathrm{TM}}\cos\theta_k$ is the component of the wave vector in the z-axis, representing the wave vectors of $InSb_1$ or $InSb_2$, singly. And $\eta_k=(\varepsilon_0/\mu_0)^{1/2}n_{\mathrm{TM}}/\cos\theta_k$ is the light conductivity, k is denoted by 1 or 2. Since ordinary mediums are not affected by applied magnetic fields, their transfer matrix is indicated as [37]:

$$\mathbf{M}_j = \begin{pmatrix} \cos(k_{jz}d_j) & -\frac{i}{\eta_j}\sin(k_{jz}d_j) \\ -i\eta_j \sin(k_{jz}d_j) & \cos(k_{jz}d_j) \end{pmatrix}, \tag{8}$$

where $k_{jz} = \omega/cn_{\mathrm{TM}}\cos\theta_j$ is the component of the wave vector in the z-axis, j can be indicated by T, Z, and M, signified by different dielectric layer materials. For JM, EWs can propagate on positive and negative scales, corresponding to different transmission matrices. This paper makes $\mathbf{M}_P$ the positive propagation transfer matrix and $\mathbf{M}_N$ is homologous to the negative transfer matrix, and their complete transfer matrix expressions follow, where $\mathbf{M}_j$ (as shown in Eq.(8)) represents the transfer matrices of medium TiO_2, ZrO_2, and SiO_2, $\mathbf{M}_{\mathrm{TM}k}$ (as shown in Eq.(7)) indicates the materials of $InSb_1$ and $InSb_2$.

The entire positive transfer matrix M_P is given as:

$$\mathbf{M}_P = \mathbf{M}_{\mathrm{T}}\mathbf{M}_{\mathrm{TM1}}\mathbf{M}_{\mathrm{Z}}(\mathbf{M}_{\mathrm{T}}\mathbf{M}_{\mathrm{M}}\mathbf{M}_{\mathrm{Z}})^6\mathbf{M}_{\mathrm{T}}\mathbf{M}_{\mathrm{TM2}}\mathbf{M}_{\mathrm{Z}}, \tag{9}$$

and the entire negative transfer matrix M_N is given as:

$$\mathbf{M}_N = \mathbf{M}_{\mathrm{Z}}\mathbf{M}_{\mathrm{TM2}}\mathbf{M}_{\mathrm{T}}(\mathbf{M}_{\mathrm{Z}}\mathbf{M}_{\mathrm{M}}\mathbf{M}_{\mathrm{T}})^6\mathbf{M}_{\mathrm{Z}}\mathbf{M}_{\mathrm{TM1}}\mathbf{M}_{\mathrm{T}}, \tag{10}$$

the results can be writen like this:

$$\mathbf{M}_r = \begin{pmatrix} M_{11} & M_{12} \\ M_{21} & M_{22} \end{pmatrix}, \tag{11}$$

where r can be indicated by P and N.

To obtain the absorptivity (A), the transmissivity (T) and the reflectivity (R) of the JM should be obtained first, which are calculated as [35]:

$$r = \frac{\eta_0(M_{11} + \eta_0 M_{12}) - (M_{21} + \eta_0 M_{22})}{\eta_0(M_{11} + \eta_0 M_{12}) + (M_{21} + \eta_0 M_{22})}, \tag{12}$$

$$t = \frac{2\eta_0}{\eta_0(M_{11} + \eta_0 M_{12}) + (M_{21} + \eta_0 M_{22})}, \tag{13}$$

$$R = |r|^2, \tag{14}$$

Table 1
The truth value table belongs to the NOR and AND logic gate (positive direction and $\theta = 0$ degrees) and the parentheses indicate the present state of the electric field and the value of A.

	In_1	In_2	Out
NOR	1 (B_1 exists)	1 (B_2 exists)	0 ($A < 0.1$)
	1 (B_1 exists)	0 (B_2 does not exist)	0 ($A < 0.1$)
	0 (B_1 does not exists)	1 (B_2 exists)	0 ($A < 0.1$)
	0 (B_1 does not exists)	0 (B_2 does not exist)	1 ($A > 0.9$)
AND	1 (B_1 exists)	1 (B_2 exists)	1 ($A > 0.9$)
	1 (B_1 exists)	0 (B_2 does not exist)	0 ($A < 0.1$)
	0 (B_1 does not exists)	1 (B_2 exists)	0 ($A < 0.1$)
	0 (B_1 does not exists)	0 (B_2 does not exists)	0 ($A < 0.1$)

$$T = |t|^2, \tag{15}$$

due to both sides of the JM being air, there is $\eta_0 = \eta_{N+1} = (\varepsilon_0/\mu_0)^{1/2} n_0/\cos\theta_0$. And then the formula for calculating can be written as [35]:

$$A = 1 - R - T. \tag{16}$$

3. Analysis and discussion

3.1. Two different logic gates

As can be seen in Fig. 1, EWs propagate along the positive z-axis. In this paper, it is a positive scale for JM when EWs start propagating from the TiO_2 layer. In contrast, when EWs start propagating from the ZrO_2, it is a negative scale. With the two external magnetic fields, B_1 and B_2, applied along the negative y-axis vertically on $InSb_1$ and $InSb_2$ respectively and the value of θ is 0 degrees, the A spectra of the positive scale NOR logic gate and negative scale AND logic gate are displayed in Fig. 2. When the magnetic field, applied vertically on $InSb_1$ or $InSb_2$, is present, it is denoted by a logic level (LL) of "1", and vice versa as "0". When a sharp AP exists and the value of absorption (A) is>0.9, it is denoted by an LL of "1", and vice versa as "0". To make a more intuitive embodiment, "In_1" stands for the state of the magnetic field B_1, "In_2" represents the state of B_2, and "Out" represents the presence of AP. Fig. 2 **(a)** illustrates this, under the condition that EWs propagate in the positive direction when both B_1 and B_2 exist, do not form an AP, and A is much smaller than 0.1 and the states are "$In_1 = 1$", "$In_2 = 1$", and "Out = 0", related to the "1 NOR 1 = 0" of the NOR logic gate. Absent the formation of an AP when B_1 exists but B_2 does not and A is substantially smaller than 0.1, that is, the states are "$In_1 = 1$", "$In_2 = 0$", and "Out = 0", related to the "1 NOR 0 = 0" of the NOR logic gate. The states are "$In_1 = 0$", "$In_2 = 1$", and "Out = 0", which are related to the "0 NOR 1 = 0" of the NOR logic gate, and do not generate an AP when B_2 exists but B_1 does not. When both B_1 and B_2 are absent, form a sharp AP and A is much>0.9, the value of it is 0.975, the frequency corresponding to AP is about 7.622 THz, and the value of Q is 232376. The states are "$In_1 = 0$", "$In_2 = 0$", and "Out = 1", related to the "0 NOR 0 = 1" of the NOR logic gate.

As can be seen from Fig. 2**(b)**, for EWs propagating in the opposite direction, appear a different logical relationship with the condition that EWs propagate in the positive direction. When both B_1 and B_2 are present, form a sharp AP and A is much>0.9, the value of it is 0.903, the frequency corresponding to AP is about 7.597 THz, and the value of Q is 205324. The states are "$In_1 = 1$", "$In_2 = 1$", and "Out = 1", related to the "1 AND 1 = 1" of the AND logic gate. The states are "$In_1 = 1$", "$In_2 = 0$",

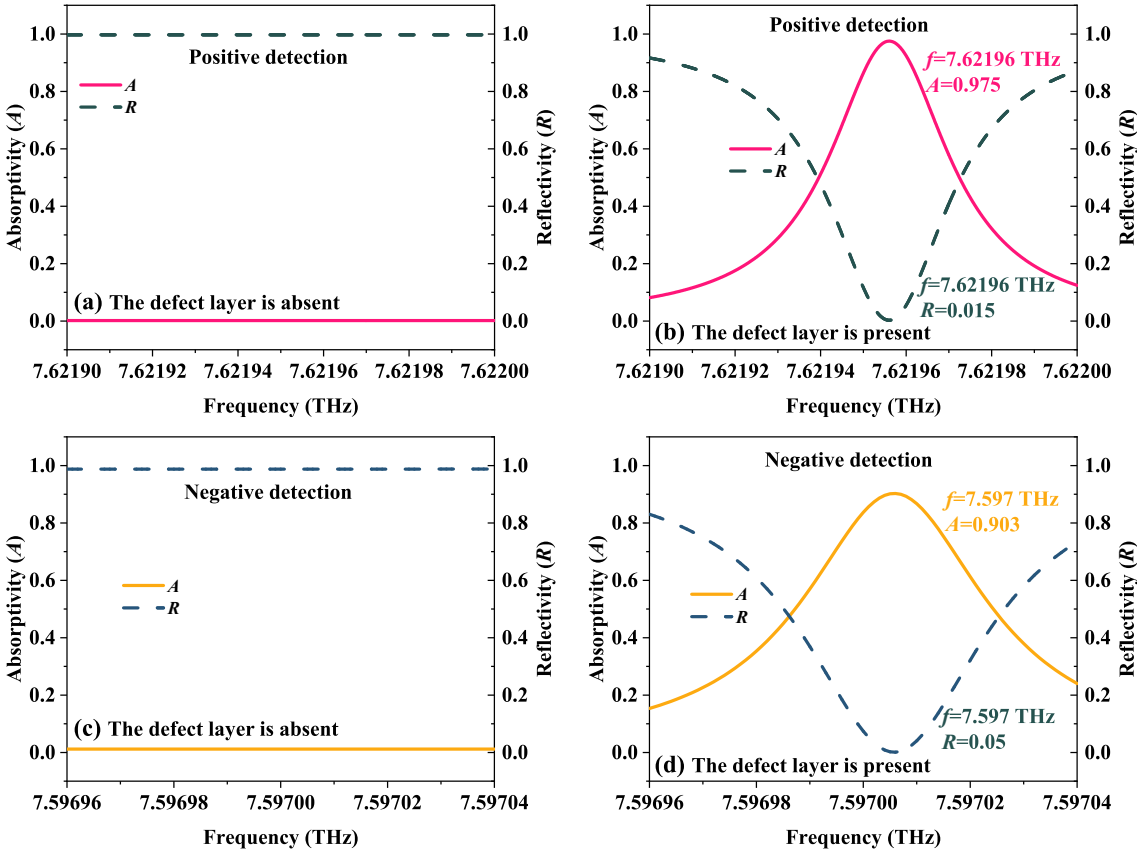

Fig. 3. The simulation of the effects of the defect layers on AP. (a) The A and R spectra before introducing defects under the condition of $B_1 = 0$ T and $B_2 = 0$ T when EWs propagate positively. (b) The A and R spectra after introducing defects under the condition of $B_1 = 0$ T and $B_2 = 0$ T when EWs propagate positively. (c) The A and R spectra before introducing defects under the condition of $B_1 = 0.65$ T and $B_2 = 1.2$ T when no defects are introduced in the structure and EWs propagate negatively. (d) The A and R spectra after introducing defects under the condition of $B_1 = 0.65$ T and $B_2 = 1.2$ T when EWs propagate negatively.

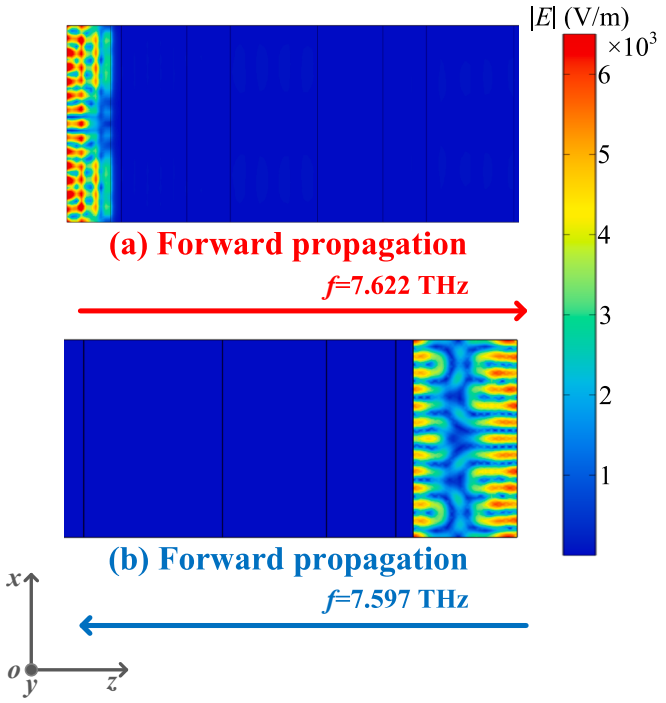

Fig. 4. The electric field distribution diagram. (a) EWs propagate positively at about f = 7.622 THz under the condition of B_1 = 0 T and B_2 = 0 T on the positive scale. (b) EWs propagate negatively at about f = 7.597 THzunder the condition of B_1 = 1 T and B_2 = 1 T on the negative scale.

and "Out = 0", which are related to the "1 AND 0 = 0" of the AND logic gate, and do not form an AP when B_1 exists but B_2 does not. AP is not generated and A is much smaller than 0.1, when B_2 exists but B_1 does not, and the states are "In_1 = 0", "In_2 = 1", and "Out = 0", related to the "0 AND 1 = 0" of the AND logic gate. If both B_1 and B_2 are absent, there is no AP and A is sizeably smaller than 0.1 and the states are "In_1 = 0", "In_2 = 0", and "Out = 0", related to the "0 AND 0 = 0"' of the NOR logic gate. As can be observed, the NOR and AND logic gate functions are strictly adhered to by the absorptivity spectra of the positive and negative directions of the JM that were developed in this work. The logical truth table is shown in Table 1.

Because there are many cases of the AP generated on the positive and negative scales of the JM designed in this paper. Among them, the introduction of the in-defect layer is one of the causes of sharp AP. When EWs propagate in the positive direction, choose the situation in which neither B_1 nor B_2 exists (B_1 = 0 T and B_2 = 0 T) to elucidate the reason of produce of AP. When an in-defect layer InSb is not added, the R and A spectra in Fig. 3**(a)** reveal that a large PBG is created between 7.6219 THz and 7.622 THz when both B_1 and B_2 are absent at the positive scale. Since the R is nearly "1″ in this range, the JM is unable to absorb EWs in this frequency range. But when InSb is introduced into the JM as the defect layer, the original PBG finally formed an A-band, and its corresponding A spectrum is shown in Fig. 3**(b)**. Similarly, when EWs propagate in the negative direction, choose the situation, both B_1 and B_2 exist (B_1 = 0.65 T and B_2 = 1.2 T), to discuss the cause of AP. From Fig. 3**(c) and (d)**, it is obvious that the PBG is broken by the introduction of the in-defect layer, and a sharp AP is formed. To more clearly monitor the TM polarization waves' propagation in JM, as shown in Fig. 4, two electric field intensity distribution maps are produced and thus illustrate the formation principle of AP. In the case of 7.622 THz, the free electrons on the surface of JM respond to the external electromagnetic field and produce a high-frequency vibration. When EWs are perpendicular to the surface of TiO_2, surface plasmon resonance can form on the surface, similar to metal surface plasmon [38,39]. Due to the existence of surface plasmon resonance, the JM can produce a sharp AP [40]. When the EWs propagate negatively at about f = 7.597 under the condition of B_1 = 1 T and B_2 = 1 T on the negative scale, the cause of producing a sharp AP is the same so. But, as can be seen in Fig. 4, the electric field intensity when EWs propagate positively is larger than the electric field intensity when EWs propagate negatively. Therefore, the A of the JM with "In1 = 1" and "In2 = 1" as the electromagnetic wave propagating in a positive direction larger than the JM with "In1 = 0" and "In2 = 0" as the electromagnetic wave propagating in a negative direction.

To explain the location and the material of the defect layer both play important roles in the phenomenon of AP when both B_1 and B_2 are absent, Fig. 5 displays the A spectra of the JM positive scale before and after changes in location and material of the defect layer. As can be seen from Fig. 5**(a)**, when the location of the defect layer is changed, the AP disappears within the frequency range from 7.6217 THz to 7.6221 THz where there would have been AP originally. Meanwhile, when the material of the defect layer is changed from InSb to TiO_2, where there would have been AP before, between 7.6217 and 7.6221 THz, there is no longer any AP. Therefore, it is clear that the location and make-up of the

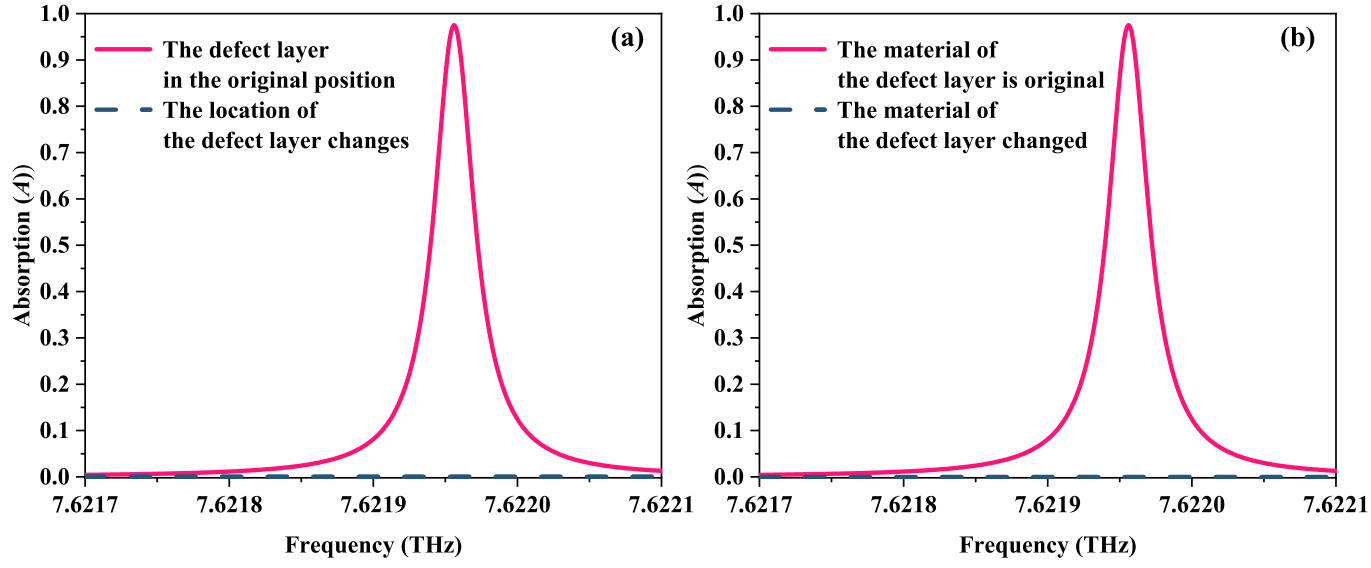

Fig. 5. The A spectra on the positive scale when B_1 = 0 T and B_2 = 0 T. (a) The change is the location of the defect layer. (b) The change is the material of the defect layer.

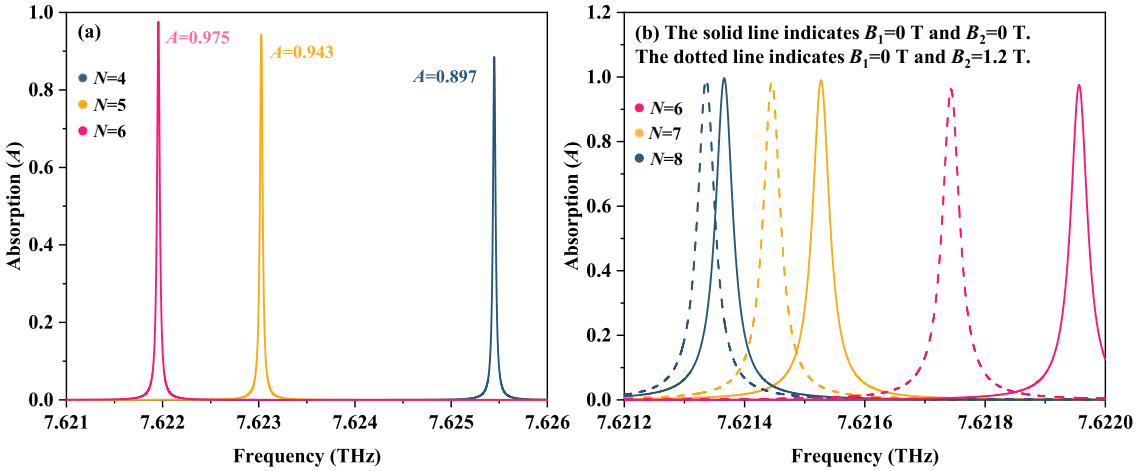

Fig. 6. The effect of the number of periods on the AP on the positive scale. (a) The *A* spectra about different *N* (the value of *N* is 4, 5, and 6) when both B_1 and B_2 do not exist. (b) The *A* spectra about different *N* (the value of *N* is 6, 7, and 8) when both B_1 and B_2 do not exist or only B_2 exists.

defect layer are essential for the development of sharp AP, and the right choice will promote efficient PBG breaking and passband formation.

Moreover, the number of dielectric layer periods (*N*) also plays an important role in the influencing factor of AP, which is exhibited in Fig. 6. Compared with the case of *N* is 4 or 5, when the value of *N* is 6, as can be seen in Fig. 6**(a)**, JM can generate a higher AP, which can improve the quality of the JM, and the value of *A* is 0.975. But as the value of *N* increases, like *N* is 7 or 8, shown in Fig. 6**(b)**, the AP, which is under the situation B_2 exists and B_1 does not, moves closer to the AP of the situation neither B_1 nor B_2 exists. So, this will cause the logic gate, mentioned above, to lose efficacy and fail. The findings show that changing the period number significantly affects how well resonant AP

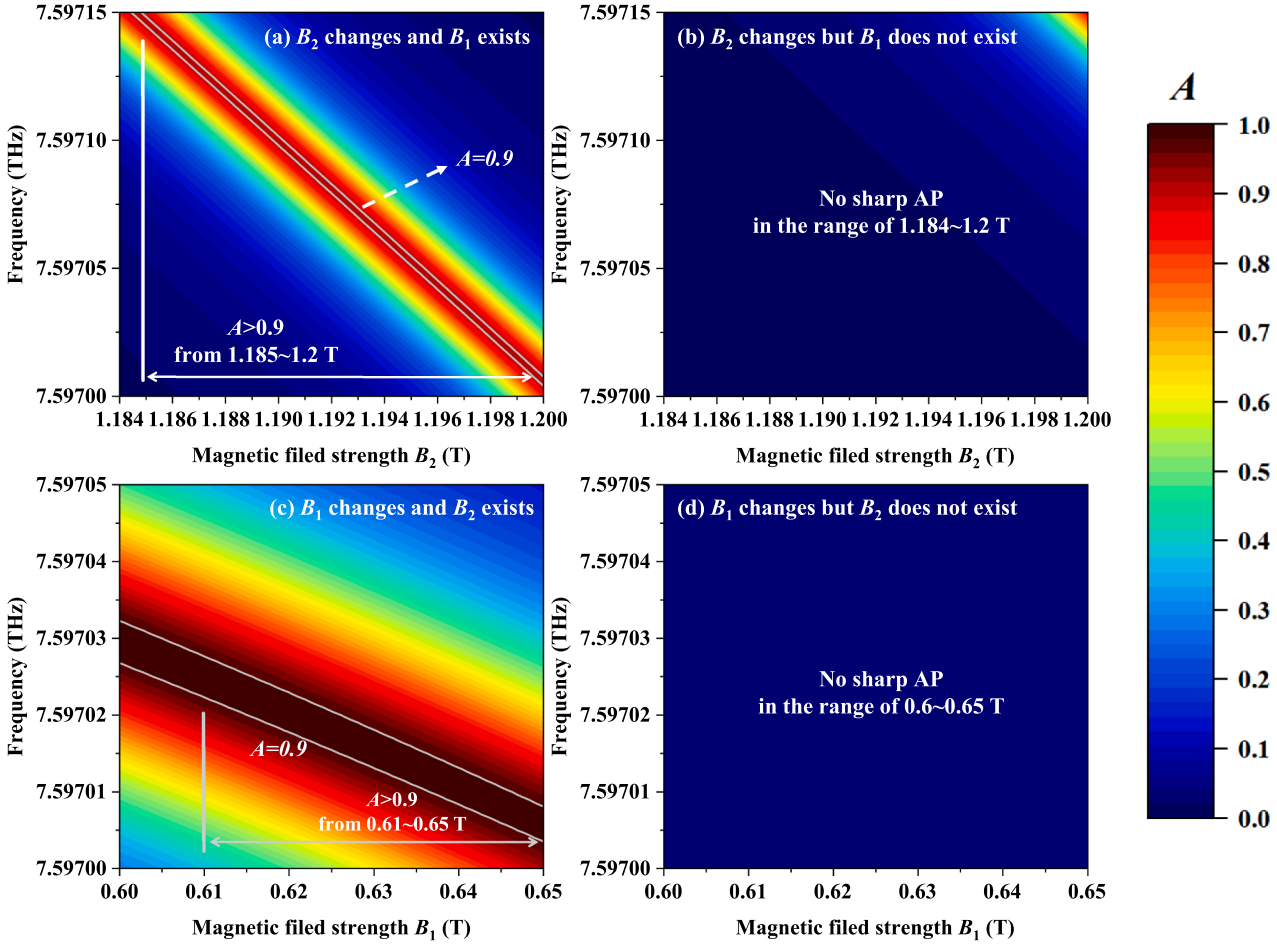

Fig. 7. The top view of AP varies with the magnetic field and the frequency (a) When B_2 changes and B_1 exists, there is a sharp AP in the range of 1.184 ~ 1.2 T. (b) When B_2 changes but B_1 does not exist, no sharp AP can be found in the range of 1.184 ~ 1.2 T. (c) When B_1 changes and B_2 exists, there is sharp AP in the range of 0.6 ~ 0.65 T. (d) When B_1 changes but B_2 does not exist, no sharp AP can be found in the range of 0.6 ~ 0.65 T.

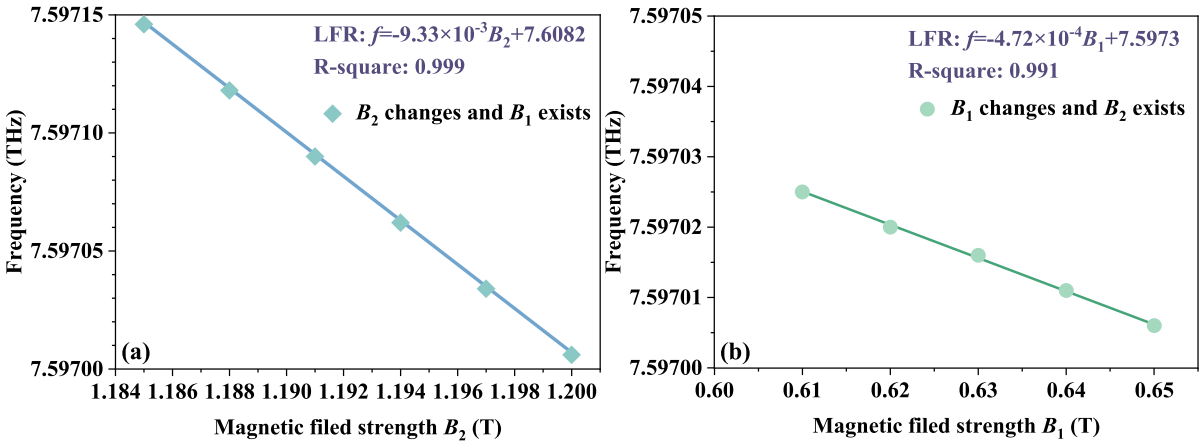

Fig. 8. LFR between the external magnetic field and FP of AP on the negative scale. (a) When B_2 changes and B_1 exists. (b) When B_1 changes and B_2 exists.

performs. This is mostly because changing the period number will change the location and strength of the local electric field, which will change the frequency of AP and the value of A.

3.2. Multiple physical quantities detection

In the production of sensors, amplitude, phase, and frequency modulation are frequently used. Frequency modulation is the most popular among them due to its practicality in experimentation and observation. It is possible to convert a signal that is difficult to observe into an easily observable photoelectric signal by creating a special linear relationship between the frequency and the variable to be measured (this physical quantity is not convenient to measure directly). The resonance frequency will move in a specific way if the value of the physical quantity being measured changes. The precise value of the physical amount to be measured can be determined by looking at the location of the AP, which is also how the sensor works. Important metrics to consider when evaluating a sensor include S, Q, FOM, and DL. A good sensor has greater S, higher Q, higher FOM, and lower DL. Corresponding definitions can be expressed as follows [41]:

$$S = \frac{\Delta f}{\Delta x}, \tag{17}$$

$$Q = \frac{f_T}{FWHM}, \tag{18}$$

$$FOM = \frac{S}{FWHM}, \tag{19}$$

$$DL = \frac{f_T}{20SQ}, \tag{20}$$

where Δf and Δx refer to the frequency and sensing physical quantity, while f_T symbolizes the frequency of AP and $FWHM$ implies the half-height width of the resonant peak.

When one of the external magnetic fields is fixed, the magnetized InSb of the negative direction of the JM can detect the external magnetic field and still maintain proper AND logic operation function in the range of detection. In the work, the transfer matrix method can be used to obtain the spatial distribution of A. Fig. 7 shows the magnetic flux density detection on the negative scale when the value of the EWs θ is 0 degrees. As can be known from Fig. 7**(a) and (b)**, the FP of the sharp AP can be changed when B_2 varies and B_1 exists ($B_1 = 0.65$ T), that is, the input LL is "$In_1 = 1$" and "$In_2 = 1$". On the opposite, the input LL is "$In_1 = 0$" and "$In_2 = 1$", when the B_1 is absent, there is no sharp AP within the range of detection. Fig. 7**(c) and (d)** displayed that the sharp AP can be changed under different frequencies when B_1 varies and B_2 exists ($B_2 = 1.2$ T), that is, the input LL is "$In_1 = 1$" and "$In_2 = 1$", and when the B_1

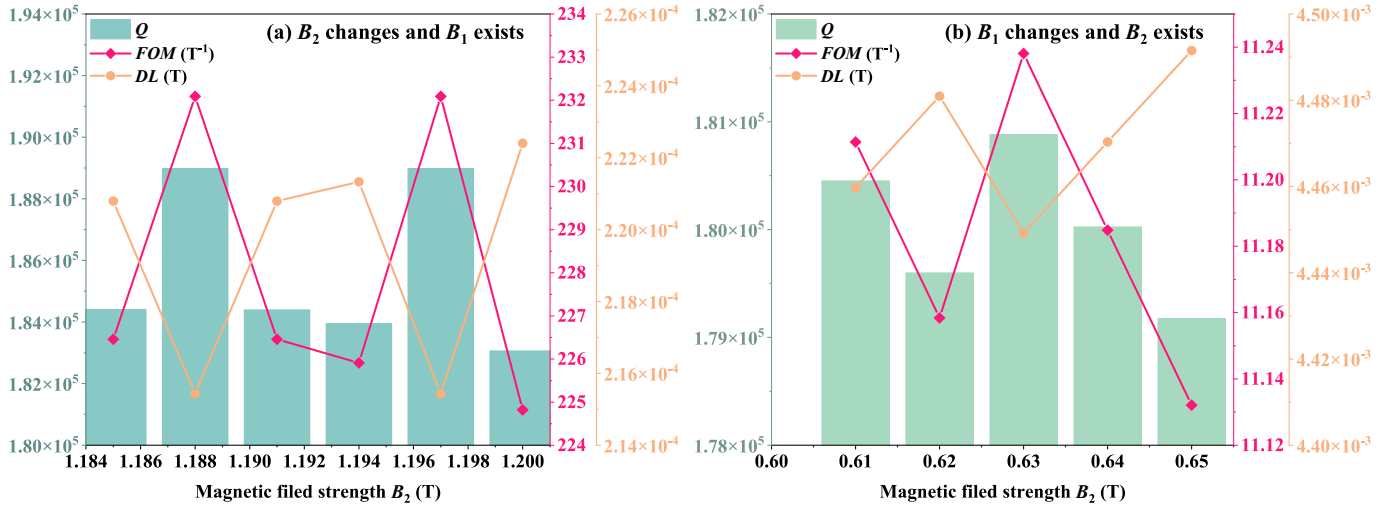

Fig. 9. The values of Q, FOM, and DL under the different magnetic field strengths on the negative scale. (a) When B_2 changes and B_1 exists. (b)When B_1 changes and B_2 exists.

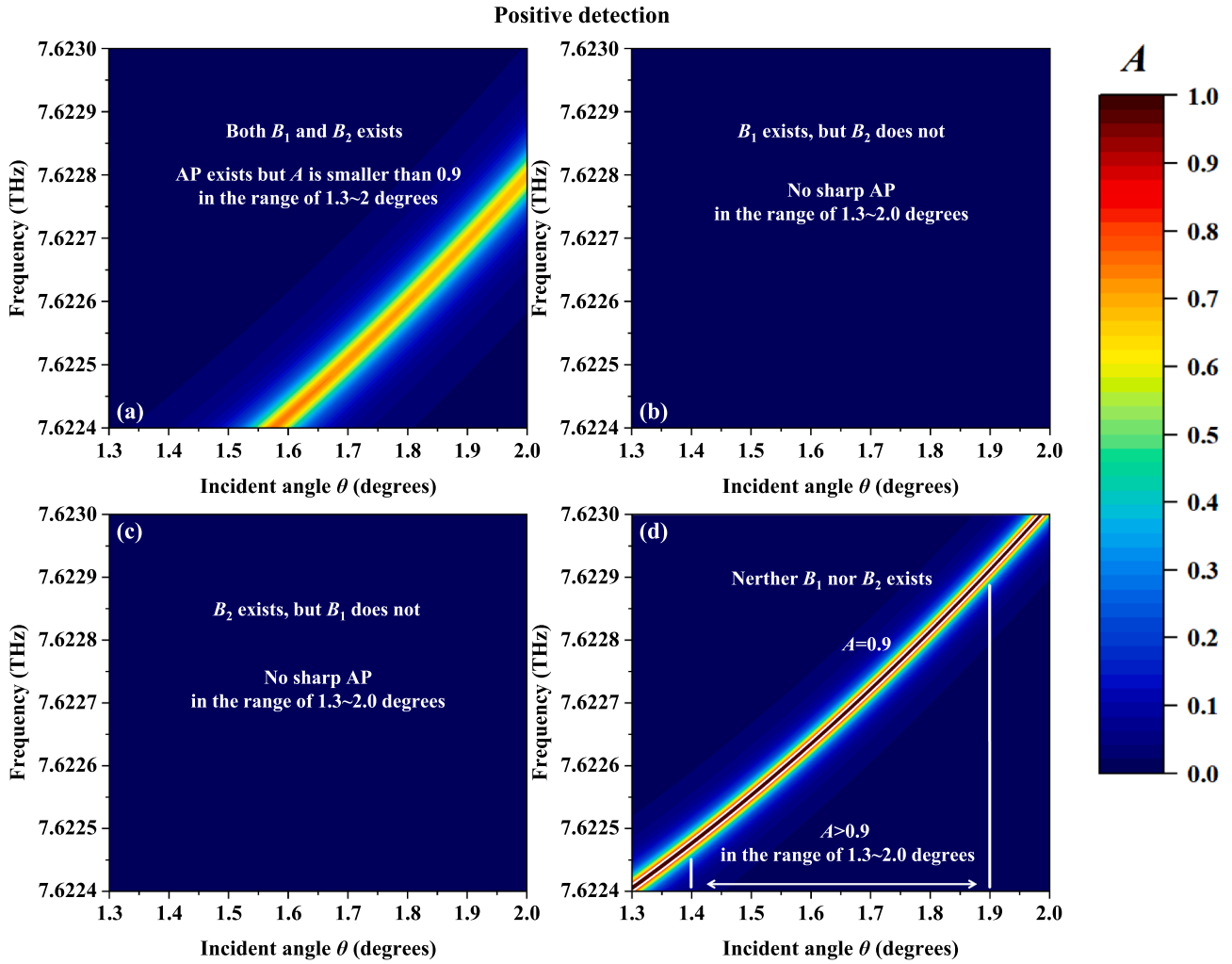

Fig. 10. The top view of AP varies with the EWs incidence angle θ and the frequency on the positive scale. (a) When both B_1 and B_2 exist, A is smaller than 0.9 in the range of 1.3 ~ 2 degrees. (b) When B_1 exists but B_2 does not, no sharp AP exist in the range of 1.3 ~ 2 degrees. (c) When B_2 exists but B_1 does not, no sharp AP exist in the range of 1.3 ~ 2 degrees. (d) When neither B_1 nor B_2 exists, there is a sharp AP ($A > 0.9$).

does not exist, that is, the input LL is "$In_1 = 1$", "$In_2 = 0$", there is not sharp AP within the range of detection. Moreover, Fig. 7**(a)** indicates that continuous AP exhibits a good linear fitting relationship (LFR) in the range of the value of B_2 from 1.185 T to 1.2 T and Fig. 7**(c)** indicates that continuous AP exhibits a good LFR in the B_1 between 0.61 T and 0.65 T. In these ranges, the values of A are>0.9, which can ensure basic detectability. Using the linear fitting method, equidistant locations along the horizontal axis are chosen to produce the LFR. In addition, to analyze the performance of LFR more clearly, the coefficient of determination R-square is used in this paper. It is an important index to demonstrate the sensor's dependability and the closer the value is to 1, the better. Fig. 8 shows the LFR between the external magnetic field and the FP of AP. Fig. 8**(a)** exhibits the LFR between B_2 and the FP of the sharp AP when B_2 varies and B_1 exists. Between the value of B_2 from 1.185 T to 1.2 T, the LFR is $f = -9.33 \times 10^{-3}B_2 + 7.6082$ and the value of S, which can be calculated through the Eq.(17), is 9.33×10^{-3} THz/T. The R-square is 0.999, which can prove that the linearity is very good to satisfy the requirement of making sensors. As well as, the LFR between B_1 and the FP of the sharp AP when B_1 varies and B_2 exists, displayed in Fig. 8**(b)**. In the range of B_1 from 0.61 T to 0.65 T, the LFR is $f = -4.72 \times 10^{-4}B_1 + 7.5973$ and the value of R-square is 0.991, which demonstrates the sensor's dependability and ability of S can reach 4.72×10^{-4} THz/T. Fig. 10 shows the values of Q, FOM, and DL for negative detection under the different magnetic field strengths. As shown in Fig. 10**(a)**, when B_2 changes and B_1 exists, the scope of Q is from 1.84×10^5 to 1.89×10^5, FOM is from 266 T^{-1} to 232 T^{-1}, and the value of DL is 2.15×10^{-4} ~ 2.23×10^{-4} T. When B_1 changes and B_2 exists, displayed by Fig. 10**(b)**, the value of Q is from 1.79×10^5 to 1.81×10^5, FOM float directly in 11.14 ~ 11.24 T^{-1}, and the range of DL is 4.45×10^{-3} ~ 4.50×10^{-3} T. These data means that the performance parameters of the JM have a certain competitive advantage.Fig. 9..

In addition, the JM, which is designed in this paper, also can detect the change of the EWs incident angle θ. Fig. 10 shows the EWs incident angle θ detection in the range of θ from 1.3 degrees to 2 degrees on the positive scale. As can be seen from Fig. 10**(a)**, when both B_1 and B_2 are absent, that is, the input LL is "$In_1 = 0$" and "$In_2 = 0$", and the output LL is "Out = 1", can get AP ($A > 0.9$) within the range of detection and AP exhibits a good LFR in the range of the value. But in Fig. 10**(b)-(d)**, in the range of detection, AP does not exist. This means that the JM cannot detect the EWs incident angle θ when the output of the NOR logic gate is not "1". It proved that the detection of θ is satisfied with the NOR logic. The negative scale of the JM can also detect θ and the range of detection is from 2.9 degrees to 3 degrees, as can be seen in Fig. 11. In the case of both B_1 and B_2 existing, the input LL is "$In_1 = 1$" and "$In_2 = 1$", and the output LL is "Out = 1". The JM can produce AP ($A > 0.9$) within the range of detection and a good LFR is built between FP and AP. But in Fig. 11**(b)-(d)**, when the output of the AND logic gate is not "1", there is no AP in the range of detection. It means the detection of θ follows AND

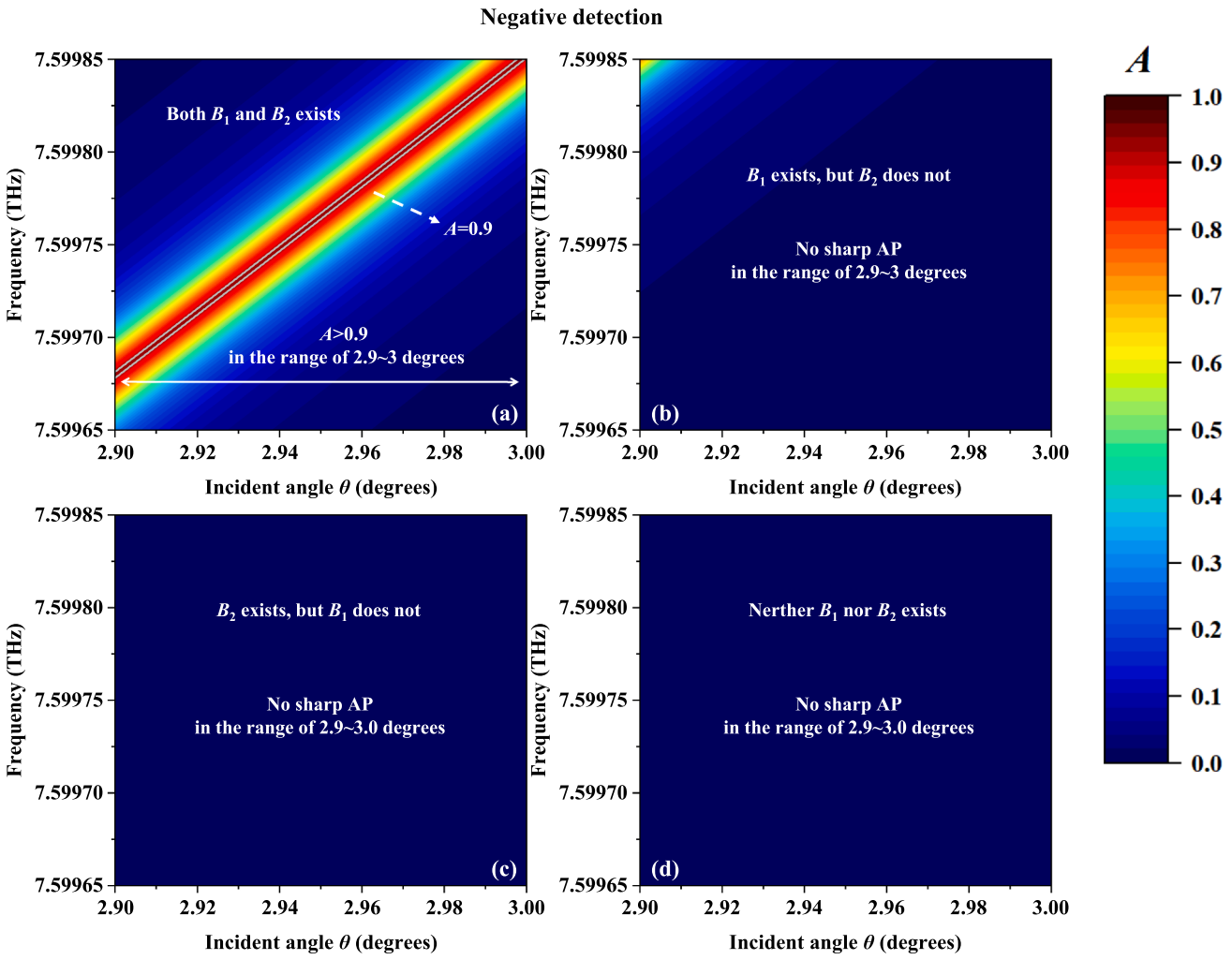

Fig. 11. The top view of AP varies with the EWs incidence angle θ and the frequency on the negative scale. (a) When both B_1 and B_2 exist, there is a sharp AP ($A >$ 0.9). (b) When B_1 exists but B_2 does not, no sharp AP exist in the range of 2.9 ~ 3 degrees. (c) When B_2 exists but B_1 does not, no sharp AP exist in the range of 2.9 ~ 3 degrees. (d) When neither B_1 nor B_2 exists, no sharp AP exists in the range of 2.9 ~ 3 degrees.

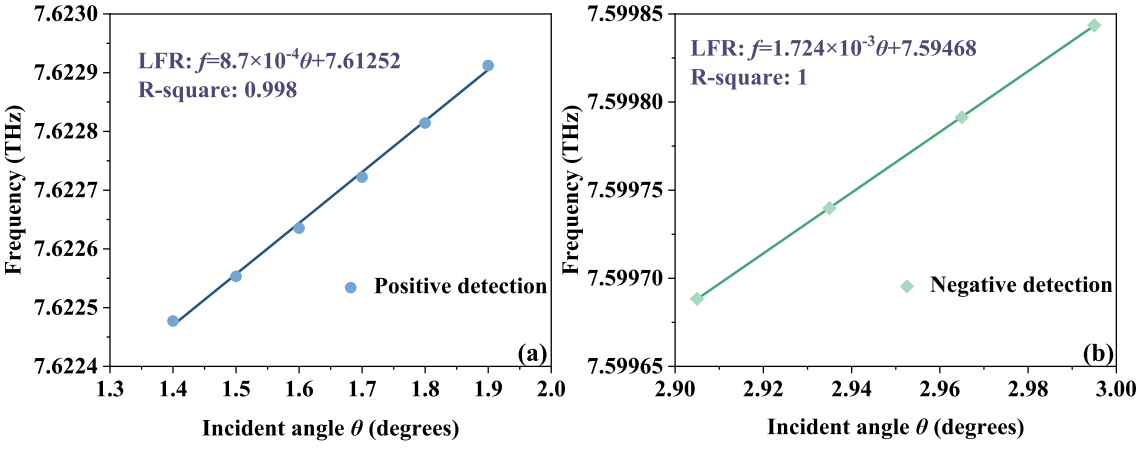

Fig. 12. LFR between the EWs incidence angle θ and the FP of AP. (a) In the case of using the positive scale to sense. (b) In the case of using the negative scale to sense.

logic gate. So that, not only the JM can sense the change of θ, but also the detection of θ can be controlled by the logic gate.

Similarly, the LFR depicted in Fig. 12 is created using the linear fitting method by selecting equidistant points along the horizontal axis. When both B_1 and B_2 are absent, Fig. 12**(a)** shows the LFR between the FP of AP and θ on the positive scale. The LFR is $f = 8.7 \times 10^{-4}\theta + 7.61252$ in the range of 1.4 ~ 1.9 degrees, and the R-square value is 0.998, demonstrating the sensor's dependability and ability of S can attain 8.7

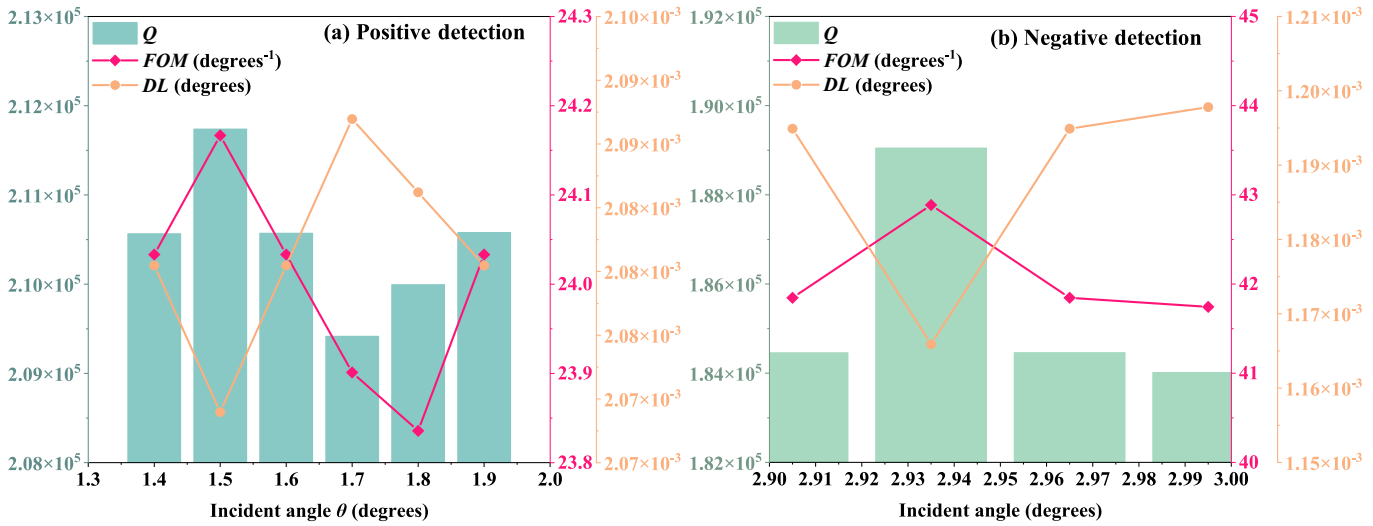

Fig. 13. The values of *Q*, *FOM*, and *DL* under the different incidence angle θ. (a) In the case of using the positive scale to sense. (b) In the case of using the negative scale to sense.

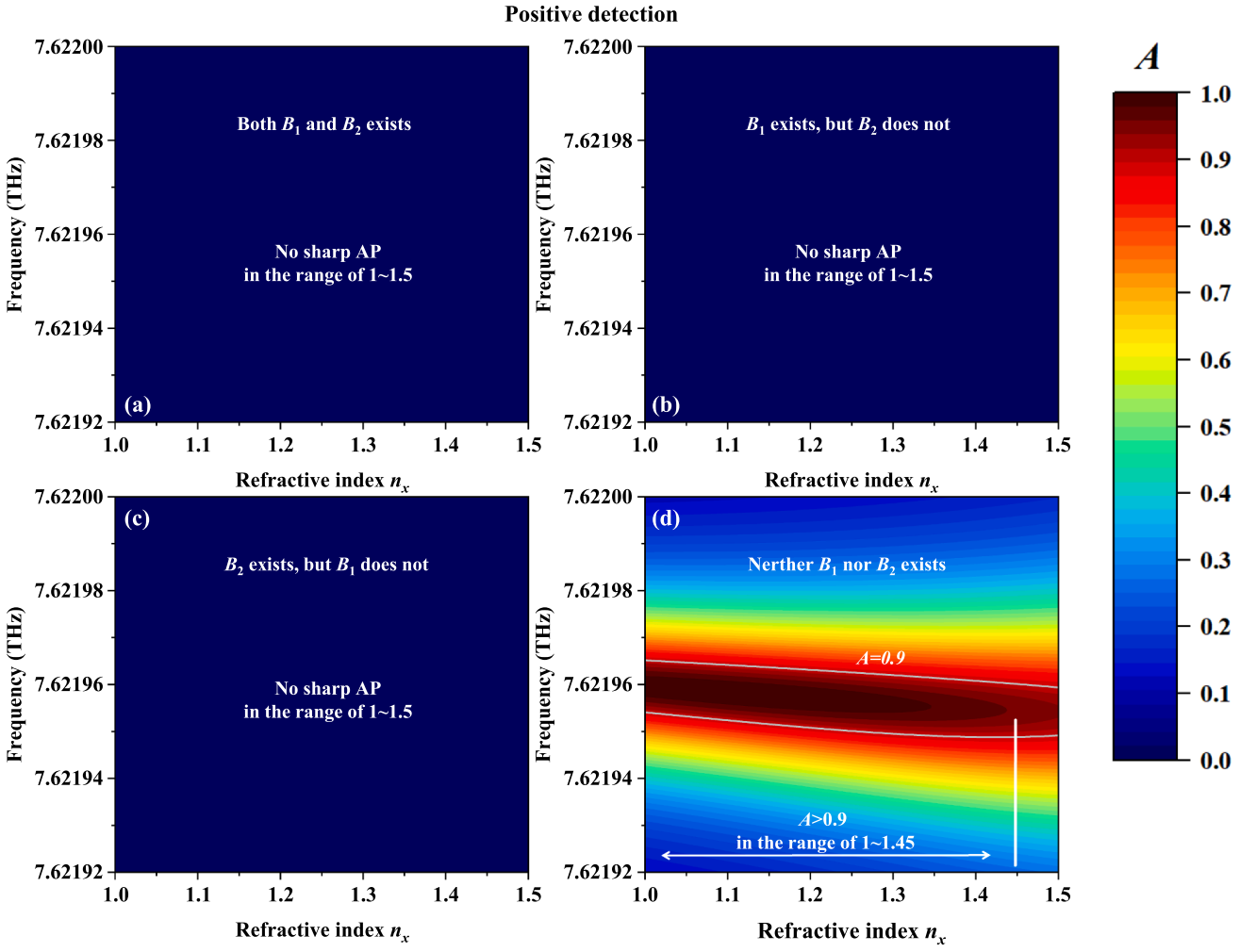

Fig. 14. The top view of AP varies with the refractive index n_x and the frequency on the positive scale. (a) When both B_1 and B_2 exist, no sharp AP exists in the range of 1 ~ 1.5. (b) When B_1 exists but B_2 does not, no sharp AP exists in the range of 1 ~ 1.5. (c) When B_2 exists but B_1 does not, no sharp AP exist in the range of 1 ~ 1.5. (d) When neither B_1 nor B_2 exists, there is a sharp AP ($A > 0.9$) in the range of 1 ~ 1.45.

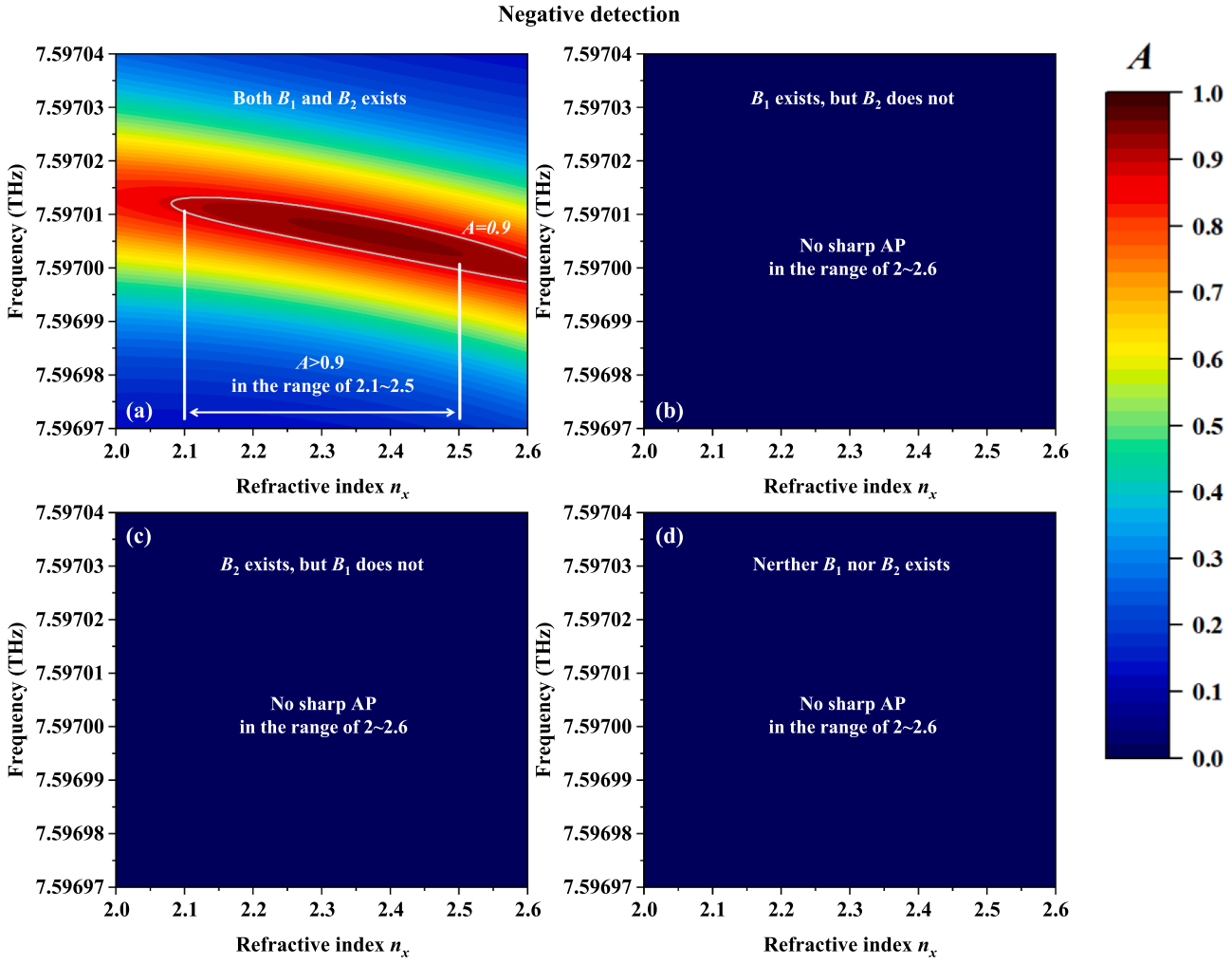

Fig. 15. The top view of AP varies with the refractive index n_x and the frequency on the negative scale. (a) When both B_1 and B_2 exist, there is a sharp AP ($A > 0.9$) in the range of 2.1 ~ 2.5. (b) When B_1 exists but B_2 does not, no sharp AP exist in the range of 2 ~ 2.6. (c) When B_2 exists but B_1 does not, no sharp AP exist in the range of 2 ~ 2.6. (d) When neither B_1 nor B_2 exists, no sharp AP exists in the range of 2 ~ 2.6.

$\times 10^{-4}$ THz/degrees. In the case of both B_1 and B_2, the LFR between FP of AP on the negative scale is exhibited in Fig. 12**(b)**. In the range of 2.9 ~ 3 degrees, the LFR is $f = 1.724 \times 10^{-3}\theta + 7.59468$, R-square is 1, and S is 1.724×10^{-3} THz/degrees.

The values of Q, FOM, and DL for positive and negative detection under the different θ can be found in Fig. 13. As shown in Fig. 13**(a)**, when the positive scale detects, the value of Q oscillates within the range of $2.09 \times 10^5 \sim 2.12 \times 10^5$, the value of FOM is from 23.85 degrees^{-1} to 24.85 degrees^{-1}, and the DL float between 2.07×10^{-3} degrees and 2.09×10^{-3} degrees. Using the negative to detect, as seen from Fig. 13**(b)**, Q is

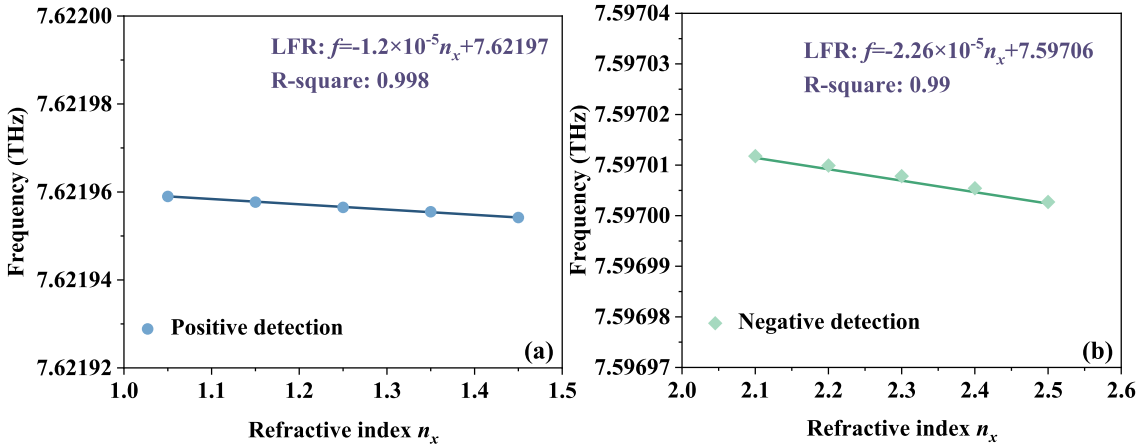

Fig. 16. LFR between the refractive index n_x and the FP of AP. (a) The positive scale is used to detect. (b) The negative scale is used to detect.

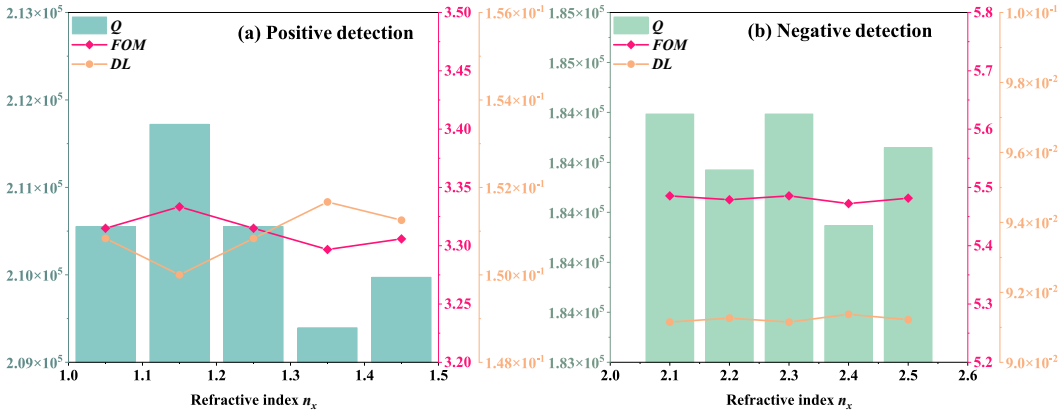

Fig. 17. The values of *Q*, *FOM*, and *DL* under the different refractive index n_x. (a) The positive scale is used to detect. (b) The negative scale is used to detect.

from 1.84×10^5 to 1.89×10^5, the scope of *FOM* is in the range of 41.7 ~ 42.7 degrees^{-1}, and the value of *DL* float between 1.165×10^{-3} degrees and 1.2×10^{-3} degrees. From these data of *Q*, *FOM*, and *DL*, what can be known is that the JM has high accuracy for angle sensing. In settings where the angle changes are too subtle to be noticed for the human eye, it can be used. For example, the shape and surface roughness of an object can be measured by detecting the EWs at a small angle. Furthermore, in medical imaging, tiny angle detection can be used to measure the changes in internal tissues or organs of the human body, like sensing the tiny angular changes in the brain of epileptic patients [42].

The identification of a substance's RI is urgently needed in the fields of biology, chemistry, physics, and others, hence there is a large selection of sensors made specifically for RI detection. The JM sensor, designed in this paper, was developed to be able to measure and detect RI in addition to the magnetic field and angle sensing detection. To study the ability of JM to detect RI and the logic operation function, a new layer, whose thickness is d_n ($d_n = d_0$), was added in front of the EWs incidence surface and its RI (n_x) is changeable.

The four logical situations in which NOR logic operates when EWs propagate positively are shown as *x*-*y* plan diagrams in Fig. 14. Fig. 14 **(d)** illustrates that in the absence of B_1 and B_2, n_x and the FP of AP create a good LFR within the RI detection range of the JM, with the value of *A* coinciding with 0.95 to 0.97 in several, which is significantly higher than 0.9 and can guarantee the LL of output is "1". When one of B_1 and B_2 exists and the other is not present, as assumed in Fig. 14**(b) and (c)**, no sharp AP is generated. Moreover, in the case of B_1 and B_2, there is no sharp AP too. This indicates that the JM for RI detection on the positive scale is strictly followed by the NOR logical operations, that is "1 NOR 1 = 0", "1 NOR 0 = 0", "0 NOR 1 = 0" and "0 NOR 0 = 1". Fig. 15 displays the situation of AND logic application when EWs propagate negatively. As can be seen in Fig. 15**(a)**, when both B_1 and B_2 are present, the FP of AP has an LFR with n_x within the RI detection range and the values of *A* are higher than 0.9, which can ensure the LL of output is "1". No sharp AP develops, when one of B_1 and B_2 is absent or both B_1 and B_2 are absent, as is assumed in Fig. 15**(b)-(d)**. It proves that the RI detection on the negative scale is strictly satisfied with the AND logic gate, which is "1 AND 1 = 1", "1 AND 0 = 0", "0 AND 1 = 0" and "0 AND 0 = 0".

Fig. 16**(a)** demonstrates objectively that the detection range of the RI of n_x is from 1.05 to 1.45 under the condition of $B_1 = 0$ T and $B_2 = 0$ T when the positive scale is used to detect n_x, and the corresponding LFR is $f = -1.2 \times 10^{-5} n_x + 7.62197$. Furthermore, the values of *S* and R-square are respectively 1.2×10^{-5} THz and 0.998, which can prove that the FP of AP has a strong LFR with n_x. As can be seen from Fig. 16**(b)**, when the detected layer is in front of the negative scale, the detection range of n_x is 2.1 ~ 2.5, when $B_1 = 0.65$ T and $B_2 = 1.2$ T, the corresponding LFR is $f = -2.26 \times 10^{-5} n_x + 7.59706$, and the *S* and R-square values are 2.26×10^{-5} THz and 0.99, demonstrating the strong LFR of AP and n_x.

Table 2
The RI corresponds to the three kinds of SWB [43].

SWB	*Escherichia coli*	*Shigella flexneri*	*Vibrio cholera*
Refractive Index	1.388 ± 0.005	1.422 ± 0.005	1.365 ± 0.005

The *Q*, *FOM*, and *DL* values related to the above two cases are demonstrated in Fig. 17. When using the positive scale to detect, as displayed in Fig. 17**(a)**, through calculation, the value of *Q* is between 2.09×10^5 and 2.12×10^5, the *FOM* value ranges from 3.3 to 3.35 and *DL* float from 0.15 and 0.152. Using the negative scale to sense the change of n_x, the *Q*, *FOM*, and *DL* values are shown in Fig. 17**(b)** and the ranges of their values separately are $1.84 \times 10^5 \sim 1.844 \times 10^5$, 5.4 ~ 5.6 and 0.09 ~ 0.092, which can meet the requirements of detection performance. The results show that the designed JM has good RI detection performance on both positive and negative detection.

Because when EWs incident forward, the RI detection range is 1.05 ~ 1.45, which is the common detection range in the field of biology. So for RI sensing, the JM, designed in this paper, can satisfy the need for some specific RI detection in some biology studies. For example, the sensing detection of the concentration of glucose aqueous solution (C_G) can be realized. The RI change of glucose in aqueous solution is comparable to the fluctuation in blood glucose levels, therefore research into the former can serve as a starting point for work on the latter. When glucose is introduced into the sensing zone as an aqueous solution, the C_G and the accompanying n_G combine to generate LFR, which is represented as [26]:

$$n_G = 1.33230545 + 0.00011889 C_G. \quad (21)$$

When the C_G is in the range of 0 ~ 500 g/L, the corresponding RI range is 1.3323 ~ 1.3918, and accurate RI detection can be achieved within the detection range of 1.05 ~ 1.45 on the positive scale. As can be seen from Fig. 16**(a)**, it can show good LFR and it is anticipated to offer a novel method for microscopic monitoring of blood glucose levels in medicine. Furthermore, the JM can also be used to measure the single waterborne bacterium (SWB) [43]. Table 2 shows the RI corresponding to the three kinds of SWB of *Escherichia coli*, *Shigella flexneri*, and *Vibrio cholera*. Their values of RI respectively are 1.388, 1.422, and 1.365. Because their RI is in the detection range on the positive scale, the JM can also be used to discriminate the three kinds of bacteria and it is expected to be more widely used in biological cell detection.

According to the research discussion above, the designed JM has excellent performance, which can satisfy the needs of EWs incident angle and RI sensing on the anteroposterior scales and magnetic field sensing on the negative scale. Moreover, the associated detection frequency varies significantly in the measurement range as EWs propagate in the opposite direction. The *S*, *Q*, and *FOM* of JM on the positive and

Table 3
The performance of the proposed JM compared with the published studies.

Reference	Janus	Multi-function	Physical quantities detection			Logic gate	
Ref. [25]	Yes	No	None			Positive	NOR
						Negative	AND
Ref. [26]	Yes	No	Positive	RI	1.33 ~ 1.35	None	
			Negative	RI	1.35 ~ 2.09		
Ref. [27]	Yes	No	Positive	Magnetic field (T)	0.14 ~ 0.22	None	
			Negative	Magnetic field (T)	0.15 ~ 0.25		
Ref. [44]	No	No	Magnetic field (T)	0.1 ~ 0.2		None	
Ref. [45]	No	No	RI	1.33 ~ 1.41		None	
This work	Yes	Yes	Magnetic field (T)	B_1 changes	0.61 ~ 0.65	Positive	NOR
				B_2 changes	1.185 ~ 1.2		
			Angle (degrees)	Positive	1.4 ~ 1.9		
				Negative	2.9 ~ 3	Negative	AND
			RI	Positive	1.05 ~ 1.45		
				Negative	2.1 ~ 2.5		

negative scales are quite different, possess good anteroposterior detection selectivity, and can detect objects with varying degrees of precision depending on the *DL*. As shown in Table 3, the NOR and AND logic operation function serves as the foundation for the physical quantity sensing function of the JM developed in this study. From the input LL "In_1", "In_2" and the corresponding output LL "Out", it can be found that it strictly follows the NOR and AND logic operation functions. Additionally, it offers a new way to convert a signal that is difficult to observe into an easily observable photoelectric signal and can be used in many detection situations. Although this paper focus on the the theoretical innovation and demonstrates the point of view of simulation-based. The professional Lab and funding cannot be had in our university Under this circumstance, our manuscript focus on theoretical innovation and innovation in research methods. Furthermore, all the results are calculated based on the equations mentioned are based on the the works that has been recognized before, and are calculated through the softwares which are recognized by the industry. So, the results in this paper are valid.

4. Conclusion

A 1-D JM, which has the functions of NOR logic gate, AND logic gate, magnetic strength sensing, angle sensing, and RI sensing, is proposed in this paper. To achieve high *Q* values, JM utilizes sharp AP ($A > 0.9$) produced by localization defect mode resonances and utilizes magnetic field regulation. The accurate physical quantity sensing function can be achieved due to the measured quantity and FP of AP having a strong linear fitting relationship and having high *S*, R-square, *FOM*, and low *DL*. For magnetic field, incident angle, and RI sensing, on the positive scale, their corresponding sensing ranges are 1.185 ~ 1.2 T, 1.4 ~ 1.9 degrees, and 1.05 ~ 1.45. On the negative scale, their corresponding sensing ranges are 0.61 ~ 0.65 T, 2.9 ~ 3 degrees, and 2.1 ~ 2.5 RIU in several. In conclusion, the suggested 1-D JM includes a multi-function of different logic gates and multiple physical quantities detection. Compared with the JM, which only has a single function and single scale, it provides a new research idea for the study and has a more promising future for theoretical research.

CRediT authorship contribution statement

Jiahao Zou: Data curation, Formal analysis, Investigation, Writing – original draft, Visualization. **Junyang Sui:** Software, Validation. **Qi Chen:** Software, Validation. **Yuxin Wei:** Software, Validation. **Hai-Feng Zhang:** Conceptualization, Methodology, Supervision, Writing – review & editing.

Declaration of Competing Interest

The authors declare that they have no known competing financial interests or personal relationships that could have appeared to influence the work reported in this paper.

Data availability

Data will be made available on request.

References

[1] J. Sui, R. Dong, S. Liao, Z. Zhao, Y. Wang, H.-F. Zhang, Janus Metastructure Based on Magnetized Plasma Material with and Logic Gate and Multiple Physical Quantity Detection, Ann. Phys. 535 (2023) 2200509.
[2] J. Sui, S. Liao, R. Dong, H.-F. Zhang, A Janus Logic Gate with Sensing Function, Annalen Der Physik. n/a (n.d.) 2200661.
[3] H. Pan, B. Li, H.F. Zhang, Anapole-excited terahertz multifunctional spoof surface plasmon polariton directional Janus metastructures, Phys. Chem. Chem. Phys. (2023).
[4] H. Da, Q. Bao, R. Sanaei, J. Teng, K.P. Loh, F.J. Garcia-Vidal, C.-W. Qiu, Monolayer graphene photonic metastructures: Giant Faraday rotation and nearly perfect transmission, Phys. Rev. B. 88 (2013), 205405.
[5] S. Park, V.P. Stinson, G.D. Boreman, T. Hofmann, Terahertz anisotropic response of additively manufactured one-dimensional photonic crystals, Opt. Lett., OL. 46 (2021) 3396–3399.
[6] X. Zeng, W. He, M.H. Frosz, A. Geilen, P. Roth, G.K.L. Wong, P.S.J. Russell, B. Stiller, Stimulated Brillouin scattering in chiral photonic crystal fiber, Photon. Res., PRJ. 10 (2022) 711–718.
[7] M.L.N. Chen, L. Chen, X. Dang, M. Li, L.J. Jiang, W.E.I. Sha, Metamaterial or Metastructural Thin Films for EM Wave Control, in: InOrganic and Organic Thin Films, John Wiley & Sons Ltd, 2021, pp. 221–255.
[8] F. Wen, S. David, X. Checoury, M.E. Kurdi, P. Boucaud, Two-dimensional photonic crystals with large complete photonic band gaps in both TE and TM polarizations, Opt. Express, OE. 16 (2008) 12278–12289.
[9] S. Yin, Z. Zhu, X. Gao, Q. Wang, J. Yuan, Y. Liu, L. Jiang, Terahertz nonreciprocal and functionality-switchable devices based on dielectric multilayers integrated with graphene and VO_2, Opt. Lett., OL. 47 (2022) 678–681.
[10] M. Shaban, A.M. Ahmed, E. Abdel-Rahman, H. Hamdy, Tunability and Sensing Properties of Plasmonic/1D Photonic Crystal, Sci Rep. 7 (2017) 41983.
[11] L. Zhu, J. Kapraun, J. Ferrara, C.J. Chang-Hasnain, Flexible photonic metastructures for tunable coloration, Optica, OPTICA. 2 (2015) 255–258.
[12] J. Ferrara, W. Yang, A. Yeh, K. Grutter, C. Chase, V. Karagodsky, D. Parekh, Y. Yue, A.E. Willner, M.C. Wu, C.J. Chang-Hasnain, Low-loss hollow-core waveguide using high-contrast sub-wavelength grating, in: High Contrast Metastructures, SPIE, 2012: pp. 90–97.
[13] J.-Y. Sui, Y.-M. Liu, H.-F. Zhang, A device of XOR logic gate and multiscale sensing based on layered topology, Waves in Random and Complex, Media (2023) 1–22.
[14] S.-S. Rao, J.-T. Zhang, H.-F. Zhang, A multifunctional and multiscale device of magnetic-controlled AND logical operation and detection based on the nonreciprocity of the magnetized InSb photonic structure, Results Phys. 31 (2021), 105058.
[15] Z. Salehnezhad, M. Soroosh, A. Farmani, Design and numerical simulation of a sensitive plasmonic-based nanosensor utilizing MoS2 monolayer and graphene, Diam. Relat. Mater. 131 (2023), 109594.
[16] A. Farmani, A. Mir, M. Bazgir, F.B. Zarrabi, Highly sensitive nano-scale plasmonic biosensor utilizing Fano resonance metasurface in THz range: Numerical study, Physica E 104 (2018) 233–240.
[17] A. Hamouleh-Alipour, A. Mir, A. Farmani, Analytical Modeling and Design of a Graphene Metasurface Sensor for Thermo-Optical Detection of Terahertz Plasmons, IEEE Sens. J. 21 (2021) 4525–4532.
[18] P. Yari, H. Farmani, A. Farmani, Steering of Guided Light with Graphene Metasurface for Refractive Index Sensing with High Figure of Merits, Plasmonics 17 (2022) 305–314.

[19] J. O'Brien, B. Patton, M. Sasaki, J. Vučković, Focus on integrated quantum optics, New J. Phys. 15 (2013), 035016.
[20] A. Politi, J.C.F. Matthews, M.G. Thompson, J.L. O'Brien, Integrated Quantum Photonics, IEEE J. Sel. Top. Quantum Electron. 15 (2009) 1673–1684.
[21] L. Ma, C. Li, L. Sun, Z. Song, Y. Lu, B. Li, Submicrosecond electro-optical switching of one-dimensional soft photonic crystals, Photon. Res., PRJ. 10 (2022) 786–792.
[22] M. Lim, S. Jin, S.S. Lee, B.J. Lee, Graphene-assisted Si-InSb thermophotovoltaic system for low temperature applications, Opt. Express, OE. 23 (2015) A240–A253.
[23] I. Kimukin, N. Biyikli, T. Kartaloglu, O. Aytur, E. Ozbay, High-speed InSb photodetectors on GaAs for mid-IR applications, IEEE J. Sel. Top. Quantum Electron. 10 (2004) 766–770.
[24] A.G. Ardakani, Tunability of absorption with temperature in the terahertz regime based on photonic crystals containing graphene and defect InSb layers, Eur. Phys. J. B. 88 (2015) 166.
[25] F. Parandin, M.M. Karkhanehchi, Terahertz all-optical NOR and AND logic gates based on 2D photonic crystals, Superlattice. Microst. 101 (2017) 253–260.
[26] S. Ghorbani, M. Sadeghi, Z. Adelpour, A highly sensitive and compact plasmonic ring nano-biosensor for monitoring glucose concentration, Laser Phys. 30 (2019), 026204.
[27] S. Atalay, A.O. Kaya, V.S. Kolat, H. Gencer, T. Izgi, One-Dimensional Magnonic Crystal for Magnetic Field Sensing, J Supercond Nov Magn. 28 (2015) 2071–2075.
[28] S. Guo, C. Hu, H. Zhang, Ultra-wide unidirectional infrared absorber based on 1D gyromagnetic photonic crystals concatenated with general Fibonacci quasi-periodic structure in transverse magnetization, J. Opt. 22 (2020), 105101.
[29] L. Xuan, X. Kong, J. Wu, Y. He, Z. Xu, A Smoothly-Connected Crescent Transverse Gradient Coil Design for 50mT MRI System, Appl Magn Reson. 52 (2021) 649–660.
[30] S. Chen, F. Fan, X. Wang, P. Wu, H. Zhang, S. Chang, Terahertz isolator based on nonreciprocal magneto-metasurface, Opt. Express, OE. 23 (2015) 1015–1024.
[31] B. Hu, Q.J. Wang, Y. Zhang, Slowing down terahertz waves with tunable group velocities in a broad frequency range by surface magneto plasmons, Opt. Express, OE. 20 (2012) 10071–10076.
[32] P.P. Trokhimchuck, Some electro-physical properties of InSb and InAs layers that were received with the help of methods of relaxed optics, in: Second International Conference on Advanced Optoelectronics and Lasers, SPIE, 2008, pp. 49–56.
[33] F. Fan, S.-J. Chang, W.-H. Gu, X.-H. Wang, A.-Q. Chen, Magnetically Tunable Terahertz Isolator Based on Structured Semiconductor Magneto Plasmonics, IEEE Photon. Technol. Lett. 24 (2012) 2080–2083.
[34] C. Nayak, C.G. Bezerra, C.H. Costa, Photonic transmission spectra in graphene-based Gaussian random multilayers, Opt. Mater. 104 (2020), 109838.
[35] B.-F. Wan, Y. Xu, Z.-W. Zhou, D. Zhang, H.-F. Zhang, Theoretical Investigation of a Sensor Based on One-Dimensional Photonic Crystals to Measure Four Physical Quantities, IEEE Sens. J. 21 (2021) 2846–2853.
[36] L. Qi, Z. Yang, F. Lan, X. Gao, Z. Shi, Properties of obliquely incident electromagnetic wave in one-dimensional magnetized plasma photonic crystals, Phys. Plasmas 17 (2010), 042501.
[37] A. Ghasempour Ardakani, T. Kalantari, H. Nadgaran, Tunable terahertz bistability with temperature in photonic crystals containing an InSb layer and coupled nonlinear defects, Eur. Phys. J. B. 88 (2015) 241.
[38] Z. Li, Y. Sun, K. Wang, J. Song, J. Shi, C. Gu, L. Liu, Y. Luo, Tuning the dispersion of effective surface plasmon polaritons with multilayer systems, Opt. Express, OE. 26 (2018) 4686–4697.
[39] A. Tanaka, S. Sakaguchi, K. Hashimoto, H. Kominami, Preparation of Au/TiO2 with Metal Cocatalysts Exhibiting Strong Surface Plasmon Resonance Effective for Photoinduced Hydrogen Formation under Irradiation of Visible Light, ACS Catal. 3 (2013) 79–85.
[40] L.-M. Tong, H.-X. Xu, Surface plasmons-mechanisms, application and perspectives, Physics 41 (9) (2012) 582–588.
[41] B.-F. Wan, Q.-Y. Wang, H.-M. Peng, H.-N. Ye, H.-F. Zhang, A Late-Model Optical Biochemical Sensor Based on OTS for Methane Gas and Glucose Solution Concentration Detection, IEEE Sens. J. 21 (2021) 21465–21472.
[42] A. Lemkaddem, A. Daducci, N. Kunz, F. Lazeyras, M. Seeck, J.-P. Thiran, S. Vulliémoz, Connectivity and tissue microstructural alterations in right and left temporal lobe epilepsy revealed by diffusion spectrum imaging, NeuroImage: Clinical. 5 (2014) 349–358.
[43] P.Y. Liu, L.K. Chin, W. Ser, T.C. Ayi, P.H. Yap, T. Bourouina, Y. Leprince-Wang, An optofluidic imaging system to measure the biophysical signature of single waterborne bacteria, Lab Chip. 14 (2014) 4237–4243.
[44] Y. Zhao, D. Wu, R.-Q. Lv, Magnetic Field Sensor Based on Photonic Crystal Fiber Taper Coated With Ferrofluid, IEEE Photon. Technol. Lett. 27 (2015) 26–29.
[45] A.K. Paul, M.d. Samiul Habib, N.H. Hai, S.M. Abdur Razzak, An air-core photonic crystal fiber based plasmonic sensor for high refractive index sensing, Opt. Commun. 464 (2020), 125556.